

**Band-gap-dependent electron and hole transport in *p*-type HgTe-CdTe superlattices**

C. A. Hoffman, J. R. Meyer, and F. J. Bartoli

*Code 6551, Naval Research Laboratory, Washington, D.C. 20375*

J. W. Han, J. W. Cook, Jr., and J. F. Schetzina

*Department of Physics, North Carolina State University, Raleigh, North Carolina 27695*

J. N. Schulman

*Hughes Research Laboratories, Malibu, California 90265*

(Received 28 June 1988)

Extensive magnetotransport and phototransport experiments have been performed on *p*-type molecular-beam-epitaxy-grown HgTe-CdTe superlattices. A mixed conduction analysis was performed in order to obtain accurate electron and hole densities and mobilities from the magnetic-field-dependent Hall and conductivity data. Band gaps determined from the temperature dependence of the intrinsic carrier density are found to systematically increase with decreasing well thickness, spanning the range 0–200 meV in the series of ten samples. Low-temperature electron and hole mobilities are in turn found to increase with decreasing gap, with both mobilities exceeding  $10^5$  cm<sup>2</sup>/Vs in zero-gap samples. The data display a number of other distinctive features, including an electron-to-hole mobility ratio near unity, an abrupt decrease in the hole (but not electron) mobility at temperatures in the range 30–50 K, and the presence of more than one species of high-mobility holes. Comparison with the results of a theoretical tight-binding calculation of the superlattice band structure indicates that all of these observations can be explained if one takes a large value for the valence-band offset (e.g., 350 meV). However, if the offset is assumed to be small (e.g., 40 meV) the band gaps for small-gap samples significantly exceed the experimental values. Furthermore, none of the qualitative features cited above are reproduced. The investigation demonstrates that, due to unusual aspects of the band structure, narrow-gap superlattices display a number of unique properties which differ considerably from those encountered in either narrow-gap alloys or III-V superlattices.

**I. INTRODUCTION**

We report a systematic experimental investigation of electron and hole transport in a series of ten *p*-type HgTe-CdTe superlattices with varying well and barrier thicknesses. Magnetotransport and phototransport measurements have been performed at temperatures between 4.2 and 300 K and magnetic fields between 100 G and 70 kG. The results of previous transport studies<sup>1,2</sup> performed at a single magnetic field are difficult to interpret because of mixed-conduction effects,<sup>3</sup> which are known to be strong in HgTe-Cd-Te superlattices over this temperature region.<sup>4</sup> In the present work, Hall and conductivity data acquired as a function of magnetic field make possible a detailed multicarrier analysis which yields accurate electron and hole densities and mobilities for the various carrier species present. The zero-temperature energy gap is derived from the temperature dependence of the intrinsic carrier density. While a similar analysis was reported previously for a single finite-gap superlattice sample,<sup>4</sup> the extensive data reported here have permitted for the first time a systematic study of electron and hole mobilities as a function of superlattice band gap. The study of hole transport has revealed mobilities with unexpected magnitudes and temperature dependencies, particularly in samples with zero band gap. The transport properties as a

function of superlattice parameters demonstrate clear trends which allow one to draw conclusions concerning the HgTe-CdTe superlattice band structure.

A multiband tight binding formalism<sup>5</sup> has been employed in the calculation of HgTe-CdTe band separations and dispersion relations as a function of superlattice parameters. The theoretical and experimental band gaps as a function of well and barrier thickness have been compared and found to yield information concerning the valence-band offset. In addition, correlations between distinctive features in the transport data and calculated band structures provide a further means of distinguishing between small and large values for the offset.

HgTe-CdTe superlattices have received a great deal of attention since 1979 when they were first suggested as a promising new material for long-wavelength infrared detectors and other electro-optical applications.<sup>6</sup> Interest in Hg-based superlattices has been further increased by recent experiments which have revealed surprising properties with potential device applications. For example, extraordinary high hole mobilities<sup>7</sup> (in excess of  $10^5$  cm<sup>2</sup>/Vs, the highest ever reported for any II VI semiconductor) and large optical nonlinearities<sup>8</sup> have been observed. These properties arise from the unique narrow-gap superlattice band structures, which are quite different from those of the more thoroughly studied III-V hetero-

structures. The materials are especially attractive because of the ability to tailor material properties for various applications by varying superlattice parameters such as barrier and well thicknesses, strain, etc. To this end, both materials-growth efforts and experimental studies will benefit significantly if the band structure and resulting electrical and optical properties can be reliably predicted. The comparison between theory and experiment made in this work provides a useful test of the predictive capability of current band-structure theory.

## II. EXPERIMENTAL PROCEDURE

### A. MBE sample growth

We have studied ten HgTe-CdTe superlattices with varying well and barrier thicknesses. All were prepared at North Carolina University in a molecular beam-epitaxy (MBE) system described in detail elsewhere.<sup>9</sup> Of the ten samples, whose layer thicknesses are listed in Table I, eight (labeled BMCCT15 to -22) were prepared in a series under very similar growth conditions. Substrates were (100) CdTe with a 2- $\mu$ m-thick buffer layer of CdTe grown by MBE at 275 °C, except for BMCCZT3, which was grown on a Cd<sub>1-x</sub>Zn<sub>x</sub>Te substrate with no buffer layer. The superlattices consisted of alternating HgTe well layers and CdTe barrier layers deposited at a substrate temperature of 175 °C. Since the entire superlattice is grown with the Hg source shutter open, the barrier layers are actually composed of the Hg<sub>1-x</sub>Cd<sub>x</sub>Te alloy ( $x \approx 0.85-0.90$ ) rather than pure CdTe.<sup>10,11</sup> The superlattice period ( $d_B + d_W$ ) is accurately determined by measuring the spacings between x-ray satellite peaks using a Blake double-crystal x-ray diffractometer. To within  $\approx 0.5$  Å, double-layer thicknesses determined in this way are almost always found to equal an integral number of lattice constants. The superlattice thickness is  $d_B + d_W$  times the number of periods, which is 200 for all of the present samples. Measurement of the total superlattice plus buffer layer thickness using a mechanical step profiler leads to an accurate determination of the buffer layer thickness and the CdTe growth rate (this rate is found to be quite reproducible). The barrier-layer growth rate is then used to determine  $d_B$  and hence  $d_W$ . Accuracy of the barrier and well thicknesses is estimated to be approximately  $\pm 1$  ML (ML denotes monolayer). As seen below, consistency of the transport properties from sample to sample supports this estimate as an upper bound on random error in the determination of layer thicknesses. For the set of ten samples, values of  $d_W$  range from 39 to 81 Å (i.e., 12–25 ML), and those of  $d_B$  from 29 to 58 Å (i.e., 9–18 ML).

### B. Experimental apparatus

van der Pauw Hall and conductivity measurements were performed on the series of superlattices as a function of magnetic field up to 70 kG, at temperatures ranging between 4.2 and 300 K. The samples were mounted in a Janis Super-Varitemp Dewar, which contains a 7 T superconducting magnet. Hall and conductivity voltages were averaged over all combinations of contacts and both

TABLE I. Summary of mixed-conduction Hall analysis for HgTe-CdTe superlattices. (ML denotes monolayers.)

Sample	Layer thickness		Electron			Hole 1		Hole 2			
	$d_W$ (Å)	$d_B$ (Å)	$n^{300K}$ (cm <sup>-3</sup> )	$\Delta T_n$ (K)	$\mu_n^{300K}$ (cm <sup>2</sup> /Vs)	$\mu_n^{\max}$ (cm <sup>2</sup> /Vs)	$\Delta T_{p_1}$ (K)	$p_1$ (cm <sup>-3</sup> )	$\Delta T_{p_2}$ (K)	$p_2$ (cm <sup>-3</sup> )	$\mu_{p_2}^{\max}$ (cm <sup>2</sup> /Vs)
BMCCT16	78	24	$2.4 \times 10^{17}$	15–300	$1.4 \times 10^4$	$1.1 \times 10^5$	4–60	$1.2 \times 10^{15}$	4–60	$3 \times 10^{15}$	$1.5 \times 10^4$
BMCCT15	81	25	$2.5 \times 10^{17}$	20–300	$1.3 \times 10^4$	$9 \times 10^4$	4–60	a	4–60	a	$1.2 \times 10^4$
BMCCT22	78	24	$1.5 \times 10^{17}$	15–300	$1.2 \times 10^4$	$4 \times 10^5$	4–40	$4 \times 10^{14}$	4–110	$2 \times 10^{15}$	$1.4 \times 10^4$
BMCCT18	61	19	$9.2 \times 10^{16}$	50–300	$6.2 \times 10^3$	$1.7 \times 10^4$	4–110	$2 \times 10^{15}$	4–110	$1.0 \times 10^4$	
BMCCT17	58	18	$7.7 \times 10^{16}$	70–300	$5.5 \times 10^3$	$1.2 \times 10^4$	4–110	$7 \times 10^{14a}$	4–110	$5 \times 10^3$	
BMCCT3	52	16	$4.5 \times 10^{16}$	70–300	$7.2 \times 10^3$	$2.4 \times 10^4$	10–60	$3 \times 10^{14}$	10–60	$3 \times 10^4$	
BMCCT21	55	17	$4.5 \times 10^{16}$	110–300	$3.6 \times 10^3$	$5 \times 10^3$	4–110	$1.3 \times 10^{15}$	4–110	$3 \times 10^3$	
BMCCTZ3	58	18	$3.7 \times 10^{16}$	120–300	$3.4 \times 10^3$	$5 \times 10^3$	4–130	$4 \times 10^{14}$	4–130	$1.5 \times 10^4$	
BMCCT20	45	14	$9 \times 10^{15}$	150–300	$2 \times 10^3$						
BMCCT19	39	12	$6 \times 10^{15}$	170–300	$5 \times 10^2$						

<sup>a</sup>Low-temperature hole densities in BMCCT15 and -17 varied with temperature (see Fig. 1). From  $p-n$  at 80 K,  $N_A - N_D \geq 7 \times 10^{14}$  cm<sup>-3</sup> in BMCCT17. Although a similar determination could not be made for BMCCT15,  $N_A - N_D \approx 10^{16}$  cm<sup>-3</sup> is estimated from carrier-heating data.

polarities of bias current and magnetic field. Automatic control of the temperature, magnetic field, and bias conditions was accomplished using a data-acquisition and processing system interfaced to a MicroVax computer. The Ohmic nature of the contacts was verified using an  $I$ - $V$  curve tracer and checked by performing all measurements at more than one bias current between 1 and 100  $\mu\text{A}$ . No significant dependence of the transport data on bias current was observed. For all samples, the Hall data appeared  $n$  type at higher temperatures, but converted to  $p$  type in the low-temperature limit. As expected, the temperature at which this type of conversion occurs varied appreciably with superlattice well thickness.

In addition to the dark transport studies, steady-state photo-Hall measurements have been performed using an experimental apparatus described in detail previously.<sup>4,12</sup> The superlattice sample was mounted in a variable-temperature Air Products closed-cycle helium refrigerator with optical access, and placed between the poles of an electromagnet with fields variable from 0 to 5 kG. Optical excitation was provided by a  $\text{CO}_2$  laser operating at 10.6  $\mu\text{m}$  with a pulse duration of 25  $\mu\text{s}$ . The laser intensity was varied over several orders of magnitude by means of calibrated attenuators. At each intensity, electrical conductivities and Hall coefficients were acquired with a Transiac transient digitizer interfaced to a computer.

### C. Data reduction

When multiple carrier species are present in a semiconductor, mixed-conduction effects complicate the interpretation of transport results.<sup>3</sup> Under these conditions, as-measured carrier densities and mobilities at a particular magnetic field differ greatly from those of the actual electrons and holes present. We define the "measured" density  $n_m$  and mobility  $\mu_m$  to be

$$n_m(B) = 1/eR_H(B) \quad (1)$$

and

$$\mu_m(B) = \sigma(B=0)R_H(B) = \sigma(B=0)/en_m(B), \quad (2)$$

where  $\sigma(B=0)$  is the zero-field conductivity,  $R_H(B)$  is the magnetic-field-dependent Hall coefficient, and  $e$  is the electronic charge. A mixed-conduction analysis can be performed to determine the densities and mobilities of the individual carrier species from the magnetic field dependencies of the conductivity and Hall coefficient, which are described by the expressions<sup>13</sup>

$$\sigma(B) = \frac{\sigma_{xx}^2 + \sigma_{xy}^2}{\sigma_{xx}} \quad (3)$$

and

$$R_H(B) = \frac{\sigma_{xy}/B}{\sigma_{xx}^2 + \sigma_{xy}^2}, \quad (4)$$

where  $\sigma_{xx}(B)$  and  $\sigma_{xy}(B)$  are the  $xx$  and  $xy$  components of the conductivity tensor, respectively. If we assume  $m$  carrier species, each with a discrete mobility, to be present in the sample,  $\sigma_{xx}$  and  $\sigma_{xy}$  can be written as

$$\sigma_{xx}(B) = \sum_{j=1}^m \frac{n_j e \mu_j}{1 + \mu_j^2 B^2}, \quad (5)$$

$$\sigma_{xy}(B) = \sum_{j=1}^m S_j \frac{n_j e \mu_j^2 B}{1 + \mu_j^2 B^2}, \quad (6)$$

where  $n_j$  and  $\mu_j$  are the density and mobility of the  $j$ th carrier species, and  $S_j$  is  $-1$  for electrons and  $+1$  for holes. It is easily seen from the denominators in these equations that higher magnetic fields cause the transport data to emphasize lower-mobility species. These equations could, of course, be generalized to account for carriers with a continuous distribution of mobilities. However, the approach employed in this work has been to assume the fewest number of discrete carrier species required for an acceptable fit to the data as a function of magnetic field and temperature.

A least-squares fit of Eqs. (5) and (6) to the magnetic field dependence of the Hall and conductivity data has been performed at each temperature for the ten  $p$ -type superlattices in the series. From this analysis, the number and type of carrier species as well as the densities and mobilities of each have been determined as a function of temperature. Table I summarizes these results along with the approximate temperature ranges over which reliable density and mobility values could be obtained for each carrier. The most notable features were found to be a high-mobility hole<sup>1</sup> which dominates the transport at low temperatures, and a high-mobility intrinsic electron which becomes important at somewhat higher temperatures. However, in samples BMCCT15, -16, and -22 the low-temperature data could not be accounted for by a single high-mobility hole species. For these samples, two high-mobility holes were assumed and the fits yielded one hole (designated  $p_1$ ) with a mobility greater than  $\approx 10^5 \text{ cm}^2/\text{V s}$  and a second hole ( $p_2$ ) with a mobility about an order of magnitude lower. It should be kept in mind that the data analysis is not sensitive enough to distinguish between two discrete hole species or, for example, some mobility distribution, with peaks at  $\mu_{p_1}$  and  $\mu_{p_2}$ .

The above analysis employs the conventional assumption that free-carrier mobilities are not appreciably altered by a magnetic field. At high fields, however, magnetic effects on the superlattice band structure can lead to a dependence of  $\mu_j$  on  $B$ . Consequently, the results reported in Table I are derived primarily from the low-field data,<sup>14</sup> i.e.,  $B < 10 \text{ kG}$ . For most samples the high-field data also indicate the presence of a low-mobility carrier, similar to results frequently reported for HgTe.<sup>15,16</sup> In a previous photo-Hall study<sup>4</sup> of sample BMCCT3, it was concluded that these carriers do not reside within the superlattice. More recent photo-Hall results on other samples in the series support this conclusion.

As shown in the table, intrinsic electrons were observed for all samples, often over a very broad temperature range. Electron densities and mobilities were obtained at temperatures as low as 15 K for thick well layers (e.g., 78  $\text{\AA}$ ), but not below 170 K for the thinnest well layers (39  $\text{\AA}$ ). Table I also lists the magnitude of the electron density and mobility at room temperature. The samples in the table are listed roughly in order of decreas-

ing  $n^{300\text{K}}$  and  $\mu_n^{300\text{K}}$ , since these quantities are known to decrease monotonically with increasing energy gap in narrow-gap semiconductors. This trend is verified below where the dependence of energy gap on superlattice well and barrier thicknesses is calculated. The maximum value of the electron mobility at low temperatures is also listed in the table. In general,  $\mu_n^{\text{max}}$  was greatest for samples with the largest well width and decreased nearly monotonically with decreasing  $d_w$ .

Table I also lists low-temperature hole densities and mobilities for the series of superlattices, as well as the approximate temperature range over which reliable values could be determined. As  $T$  increases, the growing intrinsic electron density eventually causes the fit to be insensitive to those holes present. The densities  $p_1$  and  $p_2$  are found to be nearly independent of  $T$  at low temperatures in all but two of the ten samples studied in the present investigation, as well as in  $\text{Hg}_{1-x}\text{Zn}_x\text{Te}$ - $\text{CdTe}$  results reported elsewhere.<sup>17</sup> This is somewhat surprising since bulk  $p$ -type  $\text{CdTe}$ ,  $\text{Hg}_{1-x}\text{Cd}_x$ , and  $\text{HgTe}$  samples always show freeze-out for impurity densities below the metal-insulator transition. It has been suggested<sup>17</sup> that these results are evidence for unintentional modulation doping of the superlattices. At higher temperatures,  $p_1$  and  $p_2$  increase as intrinsic carriers are thermally excited.

The extrinsic hole densities ( $p_1 + p_2 - n$ ) are plotted in Fig. 1 as a function of temperature for samples BMCCT15, -17, and -18. BMCCT18 is typical of the majority of samples, having a low-temperature hole concentration which is relatively independent of  $T$ . However, BMCCT15 and -17 are anomalous in that the zero-field conductivity steadily decreases with decreasing  $T$  down to 4.2 K and the net hole densities decrease by nearly an order of magnitude between 20 and 4.2 K. They are the first Hg-based superlattices ever reported to show significant low-temperature freeze-out of the free holes. The presence or absence of freeze-out in these samples

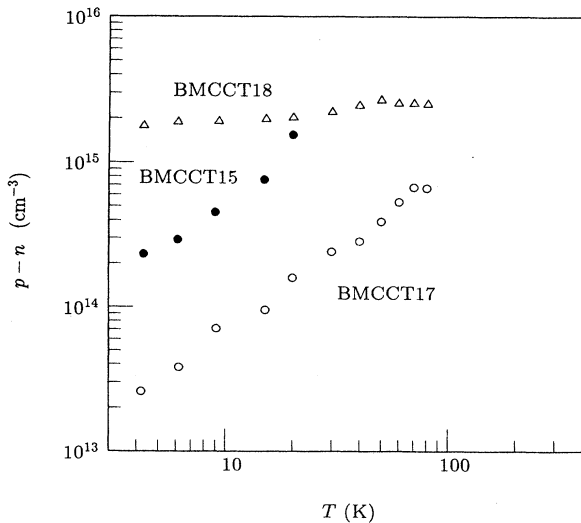


FIG. 1. Net hole densities ( $p_1 + p_2 - n$ ) vs temperature for BMCCT15, -17, and -18, as derived from the mixed-conduction analysis of the Hall and conductivity data.

can be explained within the modulation-doping picture by considering the doping levels in the barriers relative to those in the wells. Assume that the superlattices are  $p$  type and that the acceptor binding energy in the barrier is small compared to the valence-band offset. If  $N_D^{\text{well}} > (N_A - N_D)^{\text{barrier}}$  [or if  $(N_A - N_D)^{\text{barrier}} < 0$ , i.e., the barriers are  $n$  type], the barrier acceptor levels will be fully compensated and  $p$ -type modulation doping is not expected. Hence, hole freeze-out should occur as long as the acceptors in the well have a nonzero binding energy. If, on the other hand,  $N_D^{\text{well}} < (N_A - N_D)^{\text{barrier}}$ , modulation doping is expected and hole freeze-out should either be negligible or, at best, incomplete. Note that the freeze-out observed in BMCCT15 and -17 is not complete at 4.2 K. This may be due to acceptor states in the wells which are resonant or near resonant with the valence band.

For the superlattices which exhibit no freeze-out, the net acceptor concentration may be obtained from the low-temperature hole densities. We take  $N_A - N_D \approx p_1(T=0) + p_2(T=0)$ , where the low-mobility holes are ignored since they do not appear to reside in the superlattice. This leads to acceptor concentrations ranging between  $3 \times 10^{14}$  and  $4 \times 10^{15} \text{ cm}^{-3}$  in the series of samples. This approach cannot be used for the two samples showing freeze-out. However, if sample BMCCT17 is assumed to be near exhaustion at 80 K, we obtain  $N_A - N_D \approx 7 \times 10^{14} \text{ cm}^{-3}$ , which should represent a lower limit on  $N_A - N_D$ . Although it is not possible to determine  $N_A - N_D$  in this way for BMCCT15, experimental results on carrier heating for this sample<sup>18</sup> suggest that  $N_A - N_D$  is on the order of  $10^{16} \text{ cm}^{-3}$ .

If one estimates  $N_A - N_D$  from the low-temperature hole densities as discussed above, the electron density  $n$  can be used to obtain the intrinsic carrier concentration as a function of temperature from the expression

$$n_i^2 = np \approx n(N_A - N_D + n), \quad (7)$$

where it is assumed that both carriers are nondegenerate. The intrinsic carrier density is quite sensitive to the band structure near the conduction-band minimum and valence-band maximum. Although the actual superlattice band structure may be quite nonparabolic,<sup>5</sup> we can as a first-order estimate consider the conventional "law of mass action" for parabolic bands,<sup>19</sup>

$$n_i \approx 2 \left[ \frac{k_B T}{2\pi \hbar^2} \right]^{3/2} (m_n^{\text{DOS}} m_p^{\text{DOS}})^{3/4} e^{-E_g/2k_B T}, \quad (8)$$

where  $E_g(T)$  is the fundamental energy gap and the density-of-states electron and hole effective masses,  $m_n^{\text{DOS}}$  and  $m_p^{\text{DOS}}$ , must be averaged over directions parallel ( $x$ ) and perpendicular ( $z$ ) to the plane of the superlattice, i.e.,  $m^{\text{DOS}} \approx m_x^{2/3} m_z^{1/3}$ . Note that if the energy gap varies linearly with temperature, i.e.,  $E_g(T) = E_g^0 + \Gamma(T/300 \text{ K})$ , where  $E_g^0$  is the gap at zero temperature and  $\Gamma$  is the normalized temperature coefficient, the functional dependence of  $n_i$  on  $T$  is unchanged and only the multiplicative constant is altered.

Although Eq. (8) must be considered a first-order approximation, it has proved to be a useful tool for estimat-

ing energy gaps in Hg-based superlattices.<sup>4,17,20</sup> If  $n_i$  is normalized to  $T^{3/2}$  and plotted versus  $T^{-1}$  on a semilogarithmic scale, Eq. (8) predicts a straight line, whose slope yields  $E_g^0$  and whose intercept gives  $m^{\text{DOS}}$  as long as  $\Gamma$  is known. In this work, a theoretical value<sup>5</sup>  $\Gamma \approx 80$  meV is employed for the temperature shift of the gap. The method is most effective in superlattices with small band gaps since  $n_i$  can then be determined over a broad temperature range. [Since  $E_g$  enters Eq. (8) through an exponential, the sensitivity of  $n_i$  to band gap increases dramatically whenever data is available at relatively low temperatures.]

### III. EXPERIMENTAL RESULTS

Figure 2 illustrates the temperature dependence of  $n_i$  for three superlattices. For samples BMCCT21 and BMCCT17,  $n_i/T^{3/2}$  varies nearly linearly with reciprocal temperature over a fairly broad temperature range (90–300 and 70–300 K, respectively). The slope of the line for BMCCT21 gives the zero-temperature extrapolation of the energy gap  $E_g^0 \approx 80$  meV, while the intercept yields  $(m_n^{\text{DOS}} m_p^{\text{DOS}})^{1/2} \approx 0.118 m_0$ . For sample BMCCT17,  $E_g^0 \approx 54$  meV, and  $(m_n^{\text{DOS}} m_p^{\text{DOS}})^{1/2} \approx 0.119 m_0$  are obtained. On the other hand,  $n_i/T^{3/2}$  for sample BMCCT16 is nearly independent of temperature, implying a zero-temperature band gap of approximately zero. Although this sample shows a possible departure from the  $T^{3/2}$  dependence at the lowest temperatures, the maximum gap which may be inferred is less than 5 meV.

Table II lists experimental values for the zero-temperature energy gaps and density-of-states effective masses of the ten samples studied. The magnitude of  $E_g^0$  is found to vary from near zero (i.e.,  $< 8$  meV), for the three samples with the thickest well layers, to approximately 200 meV for the sample with the thinnest well. Because BMCCT19 and -20 have larger energy gaps, the intrinsic density was observable over only a limited temperature range, making the determination of the band gaps and effective masses for those samples much less ac-

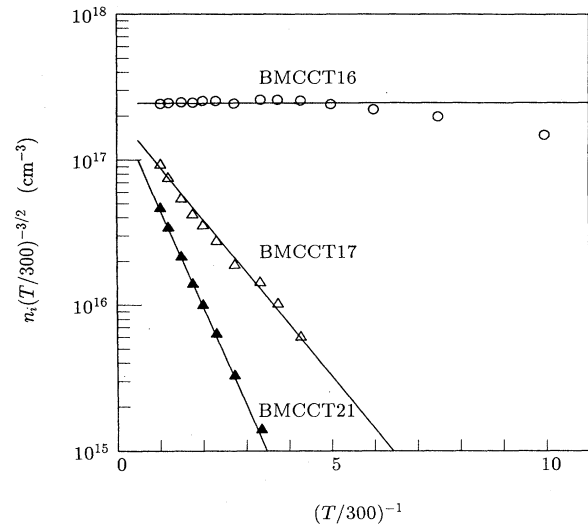


FIG. 2. Experimental intrinsic carrier densities (normalized by  $T^{3/2}$ ) vs inverse temperature for three superlattices. The curves are straight-line fits through the data.

curate. No clear systematic variation with layer thicknesses was observed for the  $(m_n^{\text{DOS}} m_p^{\text{DOS}})^{1/2}$ . Table II also gives zero-temperature energy gaps estimated from room-temperature optical transmission data for the same series of samples.<sup>21</sup> The optical gap at 300 K was assumed to correspond to the photon energy at which  $\alpha = 1000 \text{ cm}^{-1}$ .<sup>22,23</sup> The zero-temperature gap was then estimated from the relation  $E_g^0 \approx E_g^{300\text{K}} - 80$  meV. While this criterion is somewhat arbitrary, the optical band gaps agree remarkably well with recent magneto-optical measurements<sup>24</sup> on BMCCT18, -19, and -20, which give low-temperature band gaps of approximately 35, 225, and 130 meV, respectively. The optical gaps for most samples are in good agreement with those obtained from the transport data (the only significant discrepancy occurs for a superlattice with one of the thinnest well layers, for

TABLE II. Theoretical and experimental band gaps for ten HgTe-CdTe superlattices. The calculations assume that the barriers contain 15 mol % HgTe, and results are given for two different values of the valence-band offset,  $\Lambda$ . The optical gap was obtained from room-temperature absorption measurements by taking  $E_g^{300\text{K}}$  to be the photon energy at which  $\alpha \approx 1000 \text{ cm}^{-1}$  and employing the relation  $E_g^0 \approx E_g^{300\text{K}} - 80$  meV. An asterisk denotes values that are less reliable because they are based on a limited temperature range.

Sample	$d_w$ (Å)	$d_b$ (Å)	$(m_n^{\text{DOS}} m_p^{\text{DOS}})^{1/2}$	$E_g^0$ (meV)		Experiment	
				Theory		Transport	Optical
				40 meV	350 meV		
BMCCT16	78	29	0.130	5	-30	<5	-16
BMCCT15	81	32	0.132	12	-26	<8	-10
BMCCT22	78	49	0.075	51	1	<5	-3
BMCCT18	61	39	0.107	68	25	35	41
BMCCT17	58	45	0.119	89	42	54	53
BMCCT3	52	52	0.087	119	70	56	
BMCCT21	55	49	0.118	104	55	80	64
BMCCZT3	58	58	0.105	104	50	81	
BMCCT20	45	42	0.159*	132	90	186*	126
BMCCT19	39	32	0.240*	141	110	210*	190

which the uncertainty in transport  $E_g^0$  is greatest, i.e., BMCCT20). The negative optical gaps obtained for BMCCT15, -16, and -22 imply an inversion between the conduction and valence bands at low temperatures, to which the transport gaps are less sensitive.

Typical experimental transport results for one of the three nominally zero-gap superlattices are shown in Fig. 3. Temperature-dependent mobilities are given for electrons ( $\mu_n$ ) and both types of high-mobility holes ( $\mu_{p_1}$  and  $\mu_{p_2}$ ) in BMCCT15. Note the extremely high value of  $\mu_{p_1}$  at low temperatures ( $\approx 10^5$  cm<sup>2</sup>/Vs). The other two zero-gap samples listed in Table II (BMCCT16 and -22) showed similar behavior, as did two Hg<sub>1-x</sub>Zn<sub>x</sub>Te-CdTe superlattices grown at the University of Illinois at Chicago.<sup>7</sup> For these superlattices, hole mobilities as high as  $2.9 \times 10^5$  cm<sup>2</sup>/Vs are obtained from the mixed-conduction analysis, which are the highest ever reported for a II-VI semiconductor ("measured" values in excess of  $10^5$  cm<sup>2</sup>/Vs were observed in both HgTe-CdTe and Hg<sub>1-x</sub>Zn<sub>x</sub>Te-CdTe). This is especially noteworthy when one considers that hole mobilities in the bulk Hg<sub>1-x</sub>Cd<sub>x</sub>Te alloy<sup>25</sup> never exceed  $\approx 2000$  cm<sup>2</sup>/Vs. The figure also shows that  $\mu_n \approx \mu_{p_1}$  at temperatures below 30 K. In contrast, the electron-to-hole mobility ratio for bulk, narrow gap semiconductors is generally greater than 100. However, the ratio  $\mu_n/\mu_{p_1}$  increases significantly at higher temperatures. Whereas  $\mu_n$  is nearly independent of  $T$  up to 100 K,  $\mu_{p_1}$  falls by over an order of magnitude between 30 and 50 K. No hole mobilities greater than  $10^4$  cm<sup>2</sup>/Vs were observed in any of the three zero-gap samples at temperatures above 50 K. A possible explanation for this behavior in terms of the calculated band structure will be discussed in the next section.

The presence of two hole species with such high mobilities in zero-gap superlattices raises questions concerning

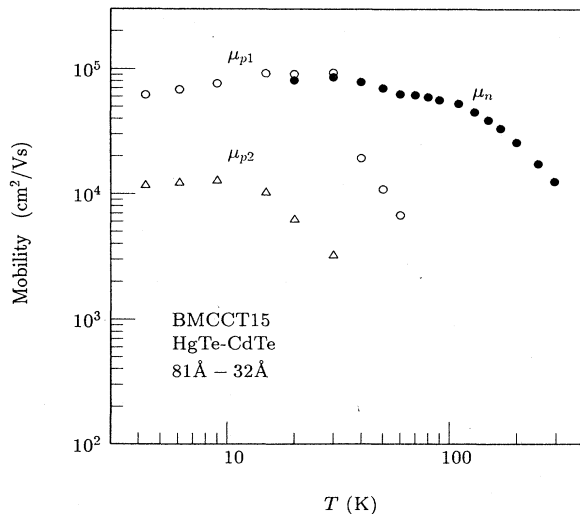


FIG. 3. Experimental electron and hole mobilities vs temperature for BMCCT15, as derived from the mixed-conduction analysis of the Hall and conductivity data.

the nature of these hole states. For example, do both species coexist within the superlattice, arising as a direct consequence of the superlattice subband structure? Or, it is possible that one of the two species resides outside the superlattice, at the surface or at an interface, for example. It has been demonstrated previously<sup>4</sup> that phototransport measurements can be instrumental in addressing such mixed-conduction questions, since they permit a determination of the net mobility as the relative concentrations of the different carrier species are varied.

Experimental photo-Hall results are illustrated in Fig. 4 for sample BMCCT16 at  $T = 12$  K and  $B = 500$  G. For a series of laser intensities, the "measured" mobility  $\mu_m$  is plotted as a function of the "measured" carrier density  $n_m$  in the region approaching type conversion. At zero laser intensity (solid circle) the transport data have a positive Hall coefficient, i.e., are  $p$  type. With optical excitation  $\Delta n$  electrons and holes are added, causing  $n_m$  to increase and  $\mu_m$  to decrease (see the open circles). Were the data continued to still higher laser intensities, the Hall coefficient would convert to  $n$  type and  $n_m$  would begin to decrease while  $\mu_m$  increased. Similar results have been reported previously for both bulk Hg<sub>1-x</sub>Cd<sub>x</sub>Te alloys<sup>12</sup> and HgTe-CdTe superlattices.<sup>4</sup>

It should be pointed out that the dominant carrier generation mechanisms are probably different for finite-gap samples such as BMCCT3 (discussed previously<sup>4</sup>) and zero-gap samples such as BMCCT16 (Fig. 4). Whereas the recombination lifetime of  $\approx 1$  ns observed for BMCCT3 was long enough to allow the generation of appreciable nonequilibrium excess carriers, strong Auger recombination generally leads to subpicosecond lifetimes in zero-gap semiconductors.<sup>26</sup> The primary effect of laser excitation on zero-gap samples is therefore carrier heat-

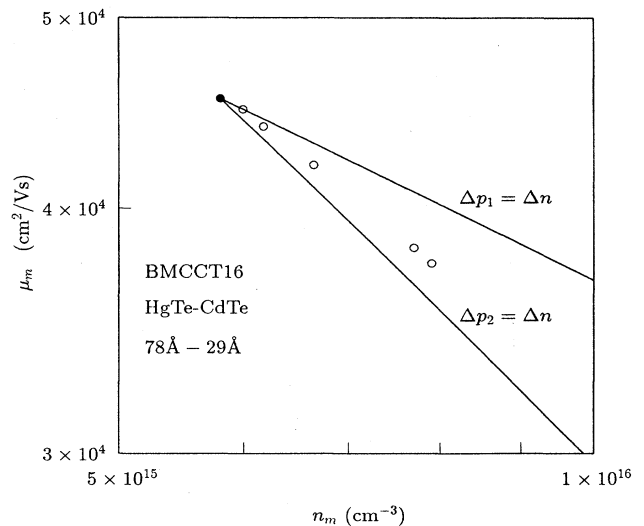


FIG. 4. Measured mobility vs measured carrier density for BMCCT16 from photo-Hall data (points), where the magnetic field was 500 G and the solid circle represents the zero-excitation limit. The curves were calculated for limiting values of the ratio  $\Delta p_1/\Delta n$ .

ing, which leads to the generation of additional intrinsic carriers. Since the electron and hole mobilities are nearly independent of temperature at 10 K and since nonequilibrium carrier and intrinsic carrier production both result in equal numbers of additional electrons and holes ( $\Delta n = \Delta p$ ), the same analysis may be used for the two methods of carrier generation. The data in Fig. 4 indicate a maximum temperature increase of  $\approx 10$  K.

One can show<sup>4</sup> that the functional form of  $\mu_m$  versus  $n_m$  is quite sensitive to the mobilities and densities of the various carriers involved in the conduction process. To understand this behavior qualitatively it is useful to consider a simplified picture involving one electron species and one hole species, at low temperatures where  $n \approx 0$  in the absence of excitation. We further ignore trapping (i.e.,  $\Delta n = \Delta p$ ) and dependencies of the electron and hole mobilities on  $\Delta n$ . One finds<sup>4</sup> that the slope  $s$  of the  $\mu_m$  versus  $n_m$  curve at low optical excitation levels is given simply by  $-\mu_n / (\mu_n + \mu_p)$ . Using this simple picture, we can predict the consequences of assuming that only one of the two holes derived from the BMCCT16 dark Hall data actually resides within the superlattice and is affected by the generation of additional carriers. If  $\Delta p_1 = \Delta n$  (and  $\Delta p_2 = 0$ ), then taking  $\mu_n / \mu_{p_1} \approx 1$  from Table I leads to  $s \approx -\frac{1}{2}$ . On the other hand, if  $\Delta p_2 = \Delta n$  ( $\Delta p_1 = 0$ ) the mobility ratio  $\mu_n / \mu_{p_2}$  is nearly 10, and  $s \approx -1$ . Since these two slopes are quite different, the photo-Hall experiment can easily distinguish between them.

Figure 4 illustrates the results of treating these same two limiting cases by a more detailed analysis<sup>4</sup> based on Eqs. (5) and (6). Values for the densities and mobilities of electrons and both types of holes in the absence of excitation have been taken from the dark Hall results as discussed above. The experimental photo-Hall data are found to fall between the two curves representing  $\Delta p_1 = \Delta n$  and  $\Delta p_2 = \Delta n$ . The best fit is obtained for  $\Delta p_1 / \Delta n = \Delta p_1 / (\Delta p_1 + \Delta p_2) \approx 0.35$ , which is quite close to the value 0.28 obtained if the excess hole densities are assumed to have the same ratio as their dark values (see Table I). These results strongly support the picture in which both hole species are coexistent in the superlattice. Photo-Hall data for the other zero-gap samples, BMCCT15 and -22, are similar and lead to the same conclusion.

Temperature-dependent electron and hole mobilities for the finite-gap samples BMCCT3 and -18 are shown in Fig. 5. The energy gaps of these samples were found from the temperature dependence of the intrinsic density to be 56 and 35 meV, respectively (see Table II). The electron mobilities behave similarly to those of BMCCT15 (Fig. 2), in that they are nearly temperature independent until  $T$  reaches about 100 K, after which they decrease in a manner qualitatively consistent with optical-phonon scattering. Note also that while the low-temperature maxima of the hole mobilities are quite close to the maximum electron mobilities,  $\mu_{p_1}$  decreases much more abruptly with increasing temperature than does  $\mu_n$  (particularly in BMCCT3). This behavior is also similar to that observed for the zero-gap superlattices, and will

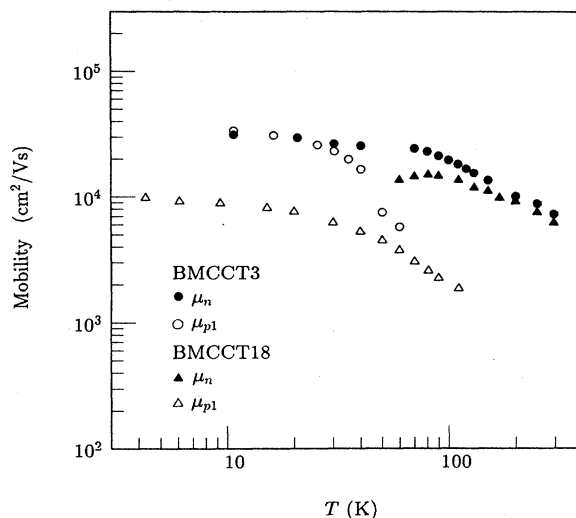


FIG. 5. Experimental electron and hole mobilities vs temperature for BMCCT3 and -18. Mobilities were derived from the mixed-conduction analysis of the dark Hall and conductivity data, except for electron mobilities at 40 K and below in BMCCT3, which were derived from photo-Hall measurements (Ref. 4).

be discussed further below in connection with the theoretical band structures.

Figure 6 illustrates maximum low-temperature mobilities for eight of the HgTe-CdTe samples from this work along with three  $\text{Hg}_{1-x}\text{Zn}_x\text{Te}$  superlattices reported elsewhere.<sup>7,17</sup> The  $\mu_n^{\text{max}}$  and  $\mu_p^{\text{max}}$  are plotted as a function of energy gap, where  $E_g$  was determined from the temperature dependence of  $n_i$ . Although there is considerable

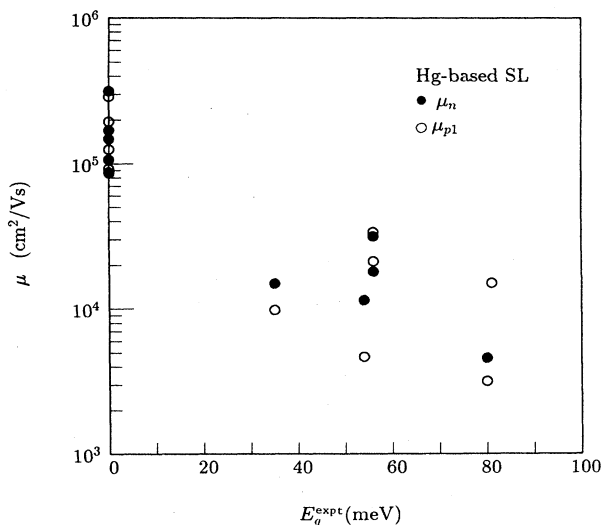


FIG. 6. Low-temperature electron and hole mobilities vs experimental band gap (as determined from the temperature dependence of the intrinsic carrier density). Data from 11 different HgTe-CdTe and  $\text{Hg}_{1-x}\text{Zn}_x\text{Te}$ -CdTe (Ref. 17) superlattices are presented.

spread in the data for samples of the same band gap, several features clearly emerge from the figure. For example, the mobilities in zero-gap superlattices are substantially greater than in those with finite gap, and both electron and hole mobilities generally decrease with increasing superlattice band gap. Also, it is found that  $\mu_n/\mu_p$  is on the order of one in almost all samples.

In the next section, band-structure calculations will be presented and related to the experimental transport results. Here we summarize some of the main features for which a connection will be made. First, values of  $E_g^0$  determined from the temperature dependence of  $n_i$  vary systematically with increasing well thickness from near zero to approximately 200 meV. Low-temperature electron and hole mobility maxima also vary nearly monotonically with well spacing (and hence band gap). In zero-gap superlattices, extremely large mobilities ( $\geq 10^5$  cm<sup>2</sup>/V s) are observed for both types of carrier. At temperatures below 30 K, the mobility ratio  $\mu_n/\mu_p$  is approximately unity, but at just slightly higher temperatures (30–50 K),  $\mu_p$  tends to decrease abruptly while  $\mu_n$  remains nearly independent of  $T$ . Finally, in zero-gap superlattices evidence is seen for more than one species of high-mobility hole.

#### IV. THEORETICAL RESULTS

##### A. Band-structure theory

We now consider theoretical results for the superlattice band structure as a function of well and barrier thicknesses, to aid in our understanding of the experimental features described above. The formalism employed is based on a multiband tight-binding theory developed by Schulman and Chang,<sup>5</sup> which includes strain. In order to approximate the experimental parameters, it will be assumed that the barriers contain approximately 15% HgTe.<sup>10,11</sup> An uncertainty of perhaps 5% in the barrier composition introduces only a few meV uncertainty in the calculated band gaps.

Figure 7 illustrates a typical dependence of the zero-temperature  $\Gamma$ -point band gap  $E_g^0$  on the number of monolayers in the well,  $N_w$ . The number of barrier monolayers,  $N_B$ , has been held constant at 9 ( $d_B = 29$  Å) and a valence-band offset of 350 meV has been assumed. As was pointed out in the earliest discussions of HgTe-CdTe superlattices by Schulman and McGill,<sup>6</sup> quantum confinement induces a finite energy gap if the well spacing is sufficiently narrow. The present theory predicts that  $E_g^0$  should steadily decrease from  $\approx 400$  meV for  $N_w = 5$  to  $\approx 3$  meV for  $N_w = 19$ . The electron and hole bands then cross and the  $\Gamma$ -point gap becomes negative. Were the valence-band offset taken to be 40 meV,  $E_g^0$  would not become negative until  $N_w \approx 25$  monolayers.

Using appropriate well and barrier thicknesses for the various superlattices studied here, we have calculated  $E_g^0$  for comparison with the experimentally determined values. Table II lists theoretical band gaps obtained for all ten samples using two different values of the valence-band offset,<sup>27</sup> 40 meV (Ref. 28) and 350 meV.<sup>29,30</sup> In the

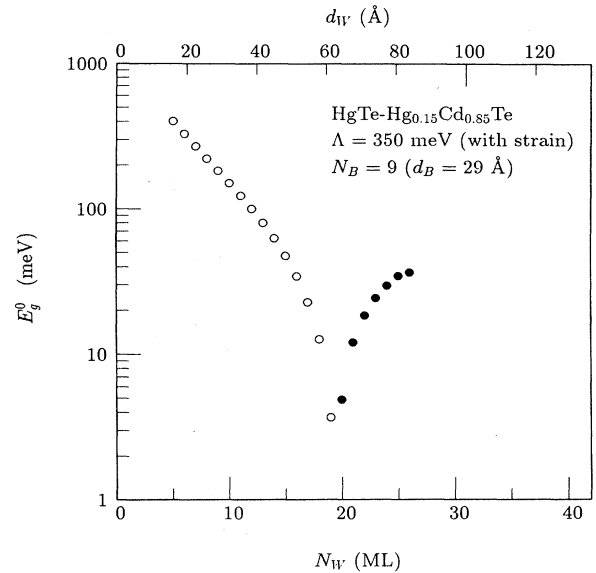


FIG. 7.  $\Gamma$ -point energy gap vs well monolayers at fixed barrier monolayers, for  $T=0$  and [100] orientation. Open circles are positive gaps while the solid circles are negative (i.e., the conduction and valence bands have crossed).

wider-well regime for which the  $n_i(T)$  determination should be most accurate ( $E_g^0 < 60$  meV), the comparison clearly favors the larger valence-band offset. In agreement with both transport and optical results, calculated values of  $E_g^0$  for samples BMCCT15, -16, and -22 are found to be less than or near zero if  $\Lambda = 350$  meV is employed. On the other hand, use of the 40-meV offset leads to finite positive gaps for all three. The clearest contrast is for sample BMCCT22, which was found by both experimental methods to have  $E_g^0$  within a few meV of zero. While the 350-meV offset gives  $E_g^0 = 1$  meV, the 40-meV offset predicts a gap of 51 meV. A difference of 50 meV is easily distinguished experimentally, as can be seen from the intrinsic density curves for BMCCT16 ( $E_g^0 \approx 0$ ) and BMCCT17 ( $E_g^0 \approx 54$  meV) in Fig. 2. Were the gap of BMCCT22 really 51 meV, then  $n_i$  at 30 K should have been over 3 orders of magnitude smaller than the observed value. A low-temperature gap of 51 meV is therefore well outside the experimental uncertainty of the  $n_i(T)$  determination for this sample. Negative gaps are predicted by Eq. (8) whenever  $\Gamma > E_g^0$  (300 K). While negative gaps have been obtained from the optical data, they have not been observed from transport measurements. This will be discussed below in terms of calculated band structures.

When samples with small, finite gaps are considered, the comparison between theory and experiment continues to strongly favor the larger valence-band offset. For BMCCT3, -17, and -18, the agreement between theory and experiment (including the magneto-optical gap<sup>24</sup> of 35 meV for sample BMCCT18) is to within 16 meV for  $\Lambda = 350$  meV, whereas 40-meV offset leads to theoretical gaps which are too high by as much as 63 meV. However, for thinner-well samples ( $E_g^0 \geq 80$  meV), the preference

for one offset over the other becomes less clear. The transport gaps for BMCCT21 and BMCCZT3 are roughly midway between the 40- and 350-meV calculated gaps, while the optical gap for BMCCT21 is more consistent with the larger offset. Transport gaps for BMCCT19 and -20 are more consistent with the 40-meV offset, although the experimental uncertainty is much higher for these samples due to the greatly restricted temperature range over which intrinsic densities could be determined. The optical gaps also favor the smaller offset, although for BMCCT19 the agreement is poor with either offset value.

In summary, the use of  $\Lambda = 350$  meV leads to good agreement between theoretical and experimental band gaps in thicker-well samples. The quantitative agreement is not as good in narrower-well samples, and it is unclear whether most of this can be attributed to the greater experimental uncertainty. Since no single value of  $\Lambda$  gives good agreement in both narrow- and wide-gap regimes, it is possible that the interpretation of these results is complicated by theoretical uncertainties related to the input parameters or assumptions of the model. These may introduce an error which varies systematically with well thickness. For example, Schulman and Chang<sup>31</sup> have pointed out that the incorporation of interdiffusion into the band-structure theory results in energy gaps which are larger than those predicted by the sharp-interface model (which is used in the present work). The presence of 1–2 monolayers of interdiffusion at each interface leads to an appreciable increase in the band gaps of samples with thin wells, but has far less effect on thick-well samples. This suggests that accounting for interdiffusion may lead to better agreement between the  $\Lambda = 350$  meV calculation and data for all band gaps. Clearly, further work is needed before this question can be resolved. Later in this section, we show that other aspects of the transport data besides the magnitudes of the energy gaps yield a strong indication of the valence-band offset.

Having established that the tight-binding calculation can approximately reproduce experimental band gaps as a function of layer thickness, we now examine the theoretical dispersion relations in order to establish correlations with the electron and hole transport results. Unfortunately, we are not presently able to compare the data to a detailed transport theory, because no comprehensive formalism incorporating the unique properties of the HgTe-CdTe superlattice band structure has yet been developed. Some of the requirements of such a theory will be briefly outlined in the next subsection.

Figure 8 shows calculated in-plane ( $k_x$ ) and perpendicular ( $k_z$ ) dispersion relations for a HgTe-CdTe superlattice with layer thicknesses  $d_W = 58$  Å and  $d_B = 29$  Å. This superlattice, which has a  $\Gamma$ -point energy gap of only 12.7 meV, is seen to have very small in-plane electron and hole effective masses near  $k_x = 0$ . Although  $m_{nz}$  is also light ( $\approx 0.014$ ), the holes are predicted to be almost dispersionless in the perpendicular direction. Since there is no single maximum in  $k_z$ , holes will populate states along the entire axis. This aspect of the perpendicular dispersion should, in fact, have a significant effect on the in-plane transport, because holes with different  $k_z$  have different in-plane masses. ( $m_{px}$  at a given  $k_z$  is roughly

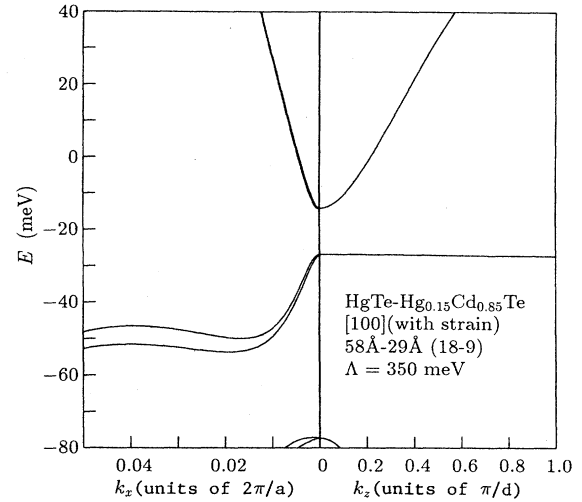


FIG. 8. Superlattice in-plane ( $k_x$ ) and growth direction ( $k_z$ ) dispersion relations for a slightly positive  $\Gamma$ -point gap ( $T=0$ ). The zero point in energy is the valence-band maximum in unstrained HgTe.

proportional to the band gap at that  $k_z$ , which in Fig. 8 varies by approximately a factor of 10 between  $k_z = 0$  and  $k_z = \pi/d$ .) Hence, the band structure shown in Fig. 8 implies that even in the limit of low temperatures and low doping levels, the highest valence band will contain coexisting holes with a wide range of in-plane effective masses. This point will be discussed further below.

Also apparent in Fig. 8 is an extreme nonparabolicity of the valence-band in-plane dispersion. For the case illustrated in the figure, the transport mass  $m^* \equiv \hbar^2 k (dk/dE)$  increases from less than 0.003 at a point 3 meV below the top of the band to essentially infinite (or negative) at energies only 23 meV farther down. Thus, the holes in narrow-gap and zero-gap Hg-based superlattices probably have a stronger nonparabolicity than free carriers in any other known material. This feature would appear to account for the experimental observation that the hole mobilities decrease dramatically at temperatures in the range 30–50 K, whereas the electron mobility is relatively independent of  $T$  below 100 K (see Figs. 3 and 5). While the holes are expected to occupy light-effective-mass states near  $k_x = 0$  at low temperatures, their average mass will become much heavier as the temperature increases and the thermal distribution spreads deeper into the band. Considering the extreme nonparabolicity of the holes near zero gap, a significant mobility decrease should not be surprising. Since the conduction band is not nearly so nonparabolic, the mobility of electrons would not be expected to be as temperature sensitive as that of the holes.

Increasing the well thickness from that used in Fig. 8 causes the electron and hole bands to cross, leading to a negative  $\Gamma$ -point gap. The band structure for a superlattice in this regime is shown in Fig. 9 ( $d_W = 84$  Å and  $d_B = 29$  Å). The most striking new feature is the electron and hole anticrossing in the  $k_z$  direction. Although the

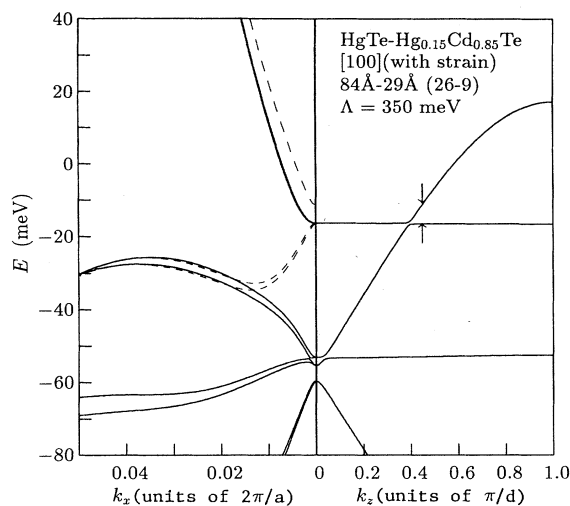


FIG. 9. Superlattice in-plane ( $k_x$ ) and growth direction ( $k_z$ ) dispersion relations for a negative  $\Gamma$ -point gap ( $T=0$ ). The dashed curves are parallel electron and hole dispersion for  $k_z=0.45\pi/d$  rather than  $k_z=0$  (see the arrows).

actual gap between the bottom of the conduction band and the top of the valence band is very near zero, it is now indirect. We define  $k_{zc}$  to be that wave vector for which the vertical separation between the electron and hole bands is a minimum. The valence-band maximum is no longer degenerate over the entire  $k_z$  axis, but only over the range  $k_z < k_z \leq \pi/d$ . However, the conduction-band minimum is now degenerate between 0 and  $k_{zc}$ , so that the electron effective mass should also vary strongly with  $k_z$ . The dashed curves in the figure illustrate the  $k_x$  dispersion relations for  $k_z$  near  $k_{zc}$ . The hole effective mass is seen to be quite small in that region, having an in-plane dispersion which differs markedly from that at  $k_z=0$ . However, near  $k_x=0$  the dashed hole band is even more nonparabolic than that in Fig. 8, and hole states with very heavy mass (in the maximum centered at  $k_x \approx 0.035$ ) lie only 11 meV below the top of the band.

The band structure shown in Fig. 9 can help to explain why negative transport gaps were not observed experimentally. The figure shows that in the zero-gap regime, the intrinsic density should be governed not by the  $\Gamma$ -point gap, but by the gap at  $k_{zc}$ . For small positive  $\Gamma$ -point gaps, where one might expect to see a negative slope, the density of states near the band edge will also decrease somewhat due to the smaller in-plane electron and hole masses. This effect may compete with the dependence of the band gap on temperature in determining the slope of the intrinsic carrier concentration.

Having shown examples of dispersion curves for both positive and negative  $\Gamma$ -point gaps, we now consider in more detail the relation between energy gap and effective mass. For the same input parameters and range of well spacings employed in obtaining the  $E_g^0$  of Fig. 7, we have calculated superlattices dispersion relations. From these we obtain in-plane electron and hole effective masses at

the  $\Gamma$  point, which are plotted in Fig. 10. Comparison with Fig. 7 shows that both  $m_n^0$  and  $m_p^0$  become quite small as the gap approaches zero, and that they are nearly proportional to  $E_g$ , especially in the region of zero gap. Recent cyclotron-resonance measurements<sup>32</sup> on BMCCT22 have, in fact, confirmed that the in-plane hole mass is extremely small, on the order of  $0.001m_0$ . Similar behavior is seen for electrons and light holes in the  $\text{Hg}_{1-x}\text{Cd}_x\text{Te}$  alloy as one approaches the semiconductor-semimetal transition.<sup>33</sup> Since almost all known scattering mechanisms yield mobilities which go inversely with effective mass (the dependence usually falls roughly between  $m^{-1/2}$  and  $m^{-5/2}$ ), the predicted proportionality of the masses to  $E_g$  is fully consistent with the experimental observation of significantly higher  $\mu_n$  and  $\mu_p$  in zero-gap samples than in those with finite band gaps. Note also from Fig. 10 that the predicted hole to electron mass ratio is less than a factor of 2 over the entire positive-gap range of  $N_W$ . This differs greatly from the mass ratios on the order of 100 found in bulk narrow-gap semiconductors. Experimentally, it was observed that the low-temperature mobility ratio is within a factor of 3 of unity in all of the samples for which the comparison could be made (see Figs. 3 and 5, Table I). This is probably related to the near equality of electron and hole masses.<sup>34</sup>

Once the  $\Gamma$ -point gap has become negative ( $N_W \geq 20$  in Fig. 10), the electron mass at  $k_z=0$  remains roughly proportional to  $|E_g|$  while the hole mass increases much more rapidly.<sup>35</sup> However, since the valence-band maximum is no longer at  $k_z=0$  (see Fig. 9), it is the states between  $k_z=k_{zc}$  and  $k_z=\pi/d$  which should most strongly affect the hole transport. It is therefore useful to examine the dependence on well width of the hole effective masses at  $k_z=k_{zc}$  and  $k_z=\pi/d$  as well as at  $k_z=0$ .

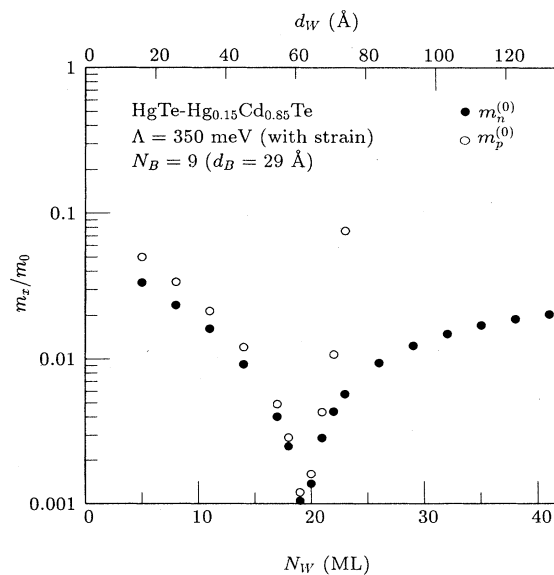


FIG. 10. In-plane electron and hole effective masses at  $k_z=0$  vs well monolayers ( $T=0$ ). The quantity plotted is an "average" density-of-states mass obtained by employing the relation  $m_x = \hbar^2 k_x^2 / 2E$ , evaluated at  $E=3$  meV.

Figure 11 displays calculated values of  $m_p^{(0)}$ ,  $m_p^{(zc)}$ , and  $m_p^{(\pi/d)}$  as a function of  $N_W$  for the same superlattice parameters employed in Figs. 7 and 10. The circles are  $\Gamma$ -point masses  $m_p^{(0)}$ , which have already been discussed in connection with Fig. 10. The squares are hole masses at the zone boundary,  $k_z = \pi/d$ . For positive values of the  $\Gamma$ -point gap ( $N_W < 20$ ),  $m_p^{(\pi/d)} > m_p^{(0)}$  because the energy gap is greater at the zone boundary than at the zone center (see Fig. 8). Both quantities decrease with increasing  $N_W$  and  $m_p^{(\pi/d)}$  continues to decrease into the negative  $\Gamma$ -point gap region ( $N_W \geq 20$ ). When the energy gap at the zone boundary finally becomes negative (at approximately 37 monolayers),  $m_p^{(\pi/d)}$  goes through a minimum and begins to increase again with  $N_W$ . In the range of  $N_W$  between which the zone-center gap is zero and that for which the zone-boundary gap is zero, the lightest hole mass is found at the band-gap minimum,  $k_{zc}$ . Values for  $m_p^{(zc)}$  are given as the triangles in the figure. The shaded region bounded by  $m_p^{(0)}$ ,  $m_p^{(zc)}$ , and  $m_p^{(\pi/d)}$  represents the range of the hole effective masses contributing to conduction for any given  $N_W$ . This “mass broadening,” which is predicted to span over an order of magnitude when  $E_g$  at the  $\Gamma$  point is near zero, may be responsible for the experimental observation that more than one type of high-mobility hole is needed to fit the field-dependent Hall and conductivity data in very small and zero-gap samples. That small masses ( $\approx 0.001m_0$ ) occur near  $k_{zc}$  for a broad range of  $N_W$  also explains why extremely high hole mobilities ( $> 10^5 \text{ cm}^2/\text{Vs}$ ) should be observable in all of the zero-gap samples, even those with negative  $\Gamma$ -point gaps. This contrasts the case of the  $\text{Hg}_{1-x}\text{Cd}_x\text{Te}$  alloy, in which the electron- and light-hole masses approach

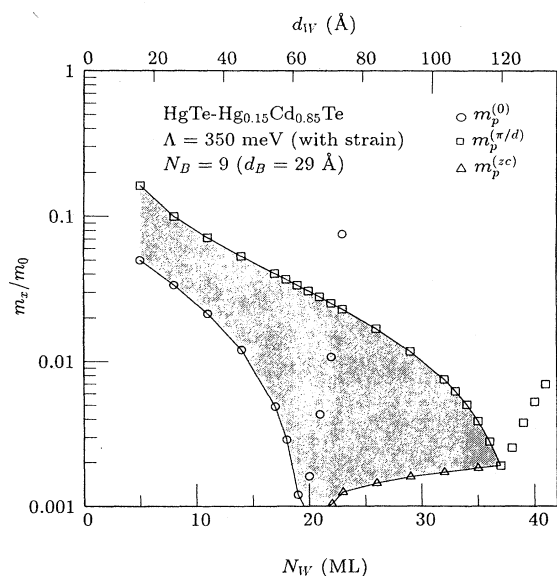


FIG. 11. In-plane hole effective masses at  $k_z=0$  ( $m_p^{(0)}$ ),  $k_z=\pi/d$  ( $m_p^{(\pi/d)}$ ), and  $k_z=k_{zc}$  ( $m_p^{(zc)}$ ) vs monolayers ( $T=0$ ). The band structure calculations predict that for a given well spacing, holes with a range of effective masses spanning the shaded region are simultaneously present in the low-temperature, low-doping limit.

zero only for  $x$  near the semiconductor-semimetal transition. Although broadening is also predicted for samples with finite positive gaps, the smaller range of effective masses may account for the result that fairly good fits could be obtained by assuming a single type of high-mobility hole in such samples. At the far right of Fig. 11 ( $N_W > 37$ ), there is no broadening because the theory predicts a single valence-band maximum at  $k_z = \pi/d$ .

In light of the fact that superlattice band structures calculated with  $\Lambda=350$  meV are remarkably consistent with the main qualitative features of the experimental transport results, it is of interest to examine the consequences of assuming a small valence-band offset, i.e., 40 meV. Figure 12 shows calculated dispersion relations for a 40-meV offset and the same layer thicknesses ( $d_W=84 \text{ \AA}$ ,  $d_B=29 \text{ \AA}$ ) as those employed for the  $\Lambda=350$  meV calculation shown in Fig. 9. The two band structures are seen to be quite different qualitatively as well as quantitatively. Instead of the negative  $\Gamma$ -point gap shown in Fig. 9, the 40-meV offset in Fig. 12 yields a small positive band gap. The in-plane electron mass does approach zero as  $E_g$  approaches zero, but the hole mass remains large<sup>5,36,37</sup> (and is relatively independent of gap). On the other hand, both electrons and holes have rapid dispersion in the growth direction, giving  $m_{nz} \approx m_{pz} \approx 0.0014$ . Moreover, the in-plane hole mass does not display any strong nonparabolicity. Band structures calculated assuming a small valence-band offset therefore fail to account for most of the distinctive features of the experimental transport data: the near equality of electron and hole mobilities in samples with a broad range of band gaps, the inverse relation between low-temperature hole mobility and band gap, the extremely high  $\mu_p$  in zero-gap samples, the apparent presence of more than one type of high-mobility hole in zero-gap samples, and the abrupt decrease of the hole-to-electron mobility ratio at temperatures between 30 and

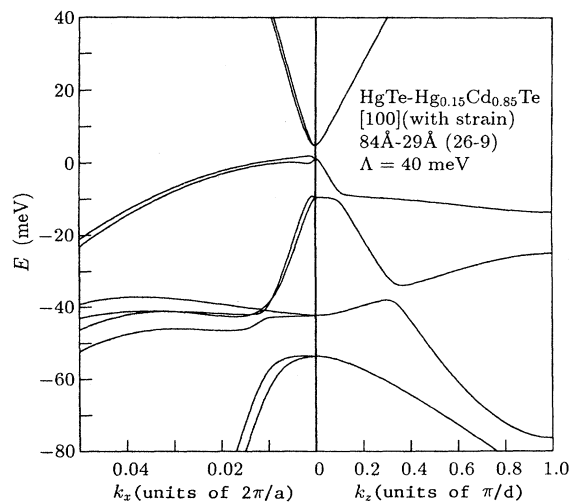


FIG. 12. Superlattice in-plane ( $k_x$ ) and growth direction ( $k_z$ ) dispersion relations for a 40-meV valence-band offset and a slightly positive  $\Gamma$ -point gap ( $T=0$ ).

50 K. To this list may be added the results of recent magneto-optical measurements by Perez *et al.*<sup>32</sup> on sample BMCCT22, which show that cyclotron-resonance hole masses are much heavier in the growth direction than they are in the plane ( $m_{pz}/m_{px} \approx 280$ ). While band structures calculated with  $\Lambda = 350$  meV (e.g., Fig. 8) predict that this ratio should be quite large, the 40-meV offset calculation illustrated in Fig. 12 yields the opposite,  $m_{pz}/m_{px} < 0.1$ .

The reason that the qualitative features of the theoretical band structures depend so strongly on the valence-band offset can be understood as follows. Consider the results of calculating HgTe-CdTe superlattice dispersion relations for a zero valence-band offset and in the absence of strain. Variation of the superlattice well width is then somewhat analogous to changing the CdTe concentration  $x$  in the  $\text{Hg}_{1-x}\text{Cd}_x\text{Te}$  alloy: the electrons and heavy holes are degenerate in the semimetallic regime while the heavy holes and light holes are degenerate in the semiconducting regime. If one considers the semiconducting case, Wu and McGill<sup>37</sup> point out that the introduction of lattice-mismatch-induced strain breaks the degeneracy of the heavy- and light-hole bands, pushing the heavy holes down and the light holes up. For  $\Lambda = 0$  the hole transport should therefore be dominated by light-hole-like states, which are characterized by rapid dispersion in the growth direction (small  $m_z$ ) but weak dispersion in the plane (large  $m_x$ ).<sup>37</sup> With the introduction of a valence-band offset, quantum confinement counters the effects of strain by moving the light holes down with respect to the heavy holes. However, an offset of 40 meV is not nearly large enough to change the ordering of the bands. In Fig. 12 the highest valence band is light-hole-like and the highest heavy-hole-like band is  $\approx 10$  meV farther down. With a large enough valence-band offset ( $\approx 200$  meV is needed), the ordering of the two bands is reversed and the transport will be dominated by heavy-hole-like states. These have very little dispersion in the growth direction (large  $m_z$ ) but mirror the electron dispersion in the plane (small  $m_x$ ).<sup>38</sup> For the band structure illustrated in Fig. 8, which is based on a 350-meV offset, the highest valence band is heavy-hole-like and the nearest light-hole band is some 50 meV farther down (it can be seen at the very bottom of the figure). Therefore, the magnitude of the valence-band offset not only affects the quantitative value of such parameters as the band gap, but also critically determines the fundamental nature of the  $k_x$  and  $k_z$  dispersion relations for holes. This is because the dominant valence band is light-hole-like for small offsets but heavy-hole-like for large offsets. The present transport data along with the recent magneto-optical data of Perez *et al.*<sup>32</sup> offer convincing evidence that the dominant valence band in our series of superlattices is heavy-hole-like.

### B. Transport theory

In the preceding sections a qualitative correlation between the tight-binding calculation and experimental Hall and conductivity data was found to yield a great deal of information concerning key aspects of the HgTe-

CdTe superlattice band structure. Unfortunately, it is currently not possible to compare the experimental results with a detailed theoretical calculation because no suitable formalism for transport in narrow-gap superlattices is yet in place. Here we briefly outline just a few of the many issues which must be confronted and unique features which must be incorporated in the development of such a theory.

Since the electron and hole effective masses in narrow- and zero-gap Hg-based superlattices are as much as 2 orders of magnitude lighter than those in the more thoroughly studied III-V heterostructure systems, the validity and usefulness of common assumptions and approximations must be reevaluated. For example, theories based on a first-order correction to the parabolic-band approximation will be highly inadequate due to the extreme nonparabolicity of both conduction and valence bands (see Figs. 8 and 9). It is therefore necessary to treat arbitrary in-plane and perpendicular dispersion relations. Similarly, since the electrons tend to have perpendicular masses ( $m_z$ ) which are of the same order of magnitude as their in-plane masses ( $m_x$ ), the transport should be considered as anisotropic in three dimensions rather than two dimensional. As was discussed in the preceding section, the theory must also account for  $k_z$ -degeneracy "mass broadening" in the valence and conduction bands.

In III-V heterostructures, magnetic-field-induced nonparabolicity may be treated as a relatively small second-order correction (in GaAs/Ga<sub>1-x</sub>Al<sub>x</sub>As heterojunctions the application of a 100-kG magnetic field leads to a  $< 10\%$  increase of the in-plane electron mass<sup>39</sup>). On the other hand, the dispersion relations illustrated in Figs. 8 and 9 suggest (and recent magneto-optical experiments<sup>32</sup> verify) that fields as low as a few kG may lead to significant nonparabolicity in samples with very narrow band gaps, and higher fields ( $\approx 20$  kG) may lead to actual inversion of the low-mass ( $k_x \approx 0$ ) and high-mass ( $k_x > 0.01$ ) regions of the valence band.

Although the electron and hole mobility data at high temperatures appear to be qualitatively consistent with what one expects due to phonon scattering, the dominant scattering mechanism at low temperatures has not yet been positively identified. Besides ionized-impurity and possibly interface-roughness scattering, electron-hole scattering should be important in narrow and zero-gap samples.<sup>40</sup> In contrast to the case of zero-gap bulk materials,<sup>16</sup> electron-hole events will strongly affect transport by both electrons and holes. The interface nature of electron and light-hole states<sup>5</sup> may play a role, and the treatment of screening by very light and extremely nonparabolic carriers may require special care. Dielectric enhancement in the zero-gap regime due to virtual band-to-band transitions<sup>41</sup> must be reformulated for the superlattice case.

As should be clear from this partial list of considerations, the unique features of narrow-gap superlattices will require the development of a comprehensive new theoretical transport formalism. Minor modification of existing theories developed for narrow-gap alloys or III-V superlattices will not be adequate. When available, such a theory will allow more detailed predictions of how the

unusual aspects of narrow-gap superlattice band structures affect the macroscopic properties. It will also be necessary to develop new approaches to such phenomena as nonlinear-optical properties, energy-relaxation mechanisms, magneto-optical transitions, recombination in indirect zero-gap materials, etc.

## V. CONCLUSIONS

A systematic investigation of carrier transport in a series of *p*-type HgTe-CdTe superlattices has been conducted. Temperature-dependent electron and hole densities and mobilities in the superlattices have been determined from magnetic-field-dependent Hall data, taking mixed conduction effects into account. The zero-temperature energy gap for each sample was determined from the temperature dependence of the intrinsic carrier density. Both electron and hole mobilities are considerably greater for zero-gap samples than for samples with a finite band gap. In all of the zero-gap samples, more than one high-mobility hole is observed at low temperatures, including a species with mobility greater than  $10^5$  cm<sup>2</sup>/V s. The hole mobility  $\mu_{p_1}$  abruptly decreases at temperatures above 30 K. In the same range the electron mobility has only a mild dependence on temperature. Theoretical band structures obtained assuming a valence-band offset of 350 meV yield not only accurate band gaps but also a number of distinctive features ob-

served in the electron and hole transport properties. For example, the low-temperature data show that  $\mu_n/\mu_{p_1} \approx 1$  in nearly all of the samples studied and both electron and hole masses are approximately proportional to  $E_g$ . The predicted "mass broadening" of holes is consistent with the need for more than one high-mobility hole to fit the zero-gap transport data. Moreover, the strong nonparabolicity near  $k_x \approx 0$  in the highest valence band is consistent with the strong temperature dependence observed for the hole mobilities. On the other hand, band structures calculated assuming a small valence-band offset (40 meV) show poor correlation with the data. Although many of the unusual band-structure features predicted by theory, such as the "indirect" band alignment at zero gap and the secondary valence-band maximum near  $k_x \approx 0.035$ , are yet to be verified experimentally, it appears that type-III Hg-based superlattices in the narrow- and zero-gap regimes are unique materials with properties quite distinct from either Hg-based alloys or III-V superlattices.

## ACKNOWLEDGMENTS

The authors are grateful to R. J. Wagner for many useful discussions. This research was supported by the Strategic Defense Initiative Office of Innovative Science and Technology and managed by the U. S. Naval Research Laboratory.

- <sup>1</sup>J. P. Faurie, M. Boukerche, S. Sivananthan, J. Reno, and C. Hsu, *Superlatt. Microstruct.* **1**, 237 (1985).
- <sup>2</sup>K. A. Harris, S. Hwang, Y. Lansari, J. W. Cook, Jr., J. F. Schetzina, and M. Chu, *J. Vac. Sci. Technol. A* **5**, 3085 (1987).
- <sup>3</sup>For example, E. H. Putley, *The Hall Effect and Semiconductor Physics* (Dover, New York, 1960), p. 85.
- <sup>4</sup>C. A. Hoffman, J. R. Meyer, E. R. Youngdale, J. R. Lindle, F. J. Bartoli, K. A. Harris, J. W. Cook, Jr., and J. F. Schetzina, *Phys. Rev. B* **37**, 6933 (1988).
- <sup>5</sup>J. N. Schulman and Y.-C. Chang, *Phys. Rev. B* **33**, 2594 (1986).
- <sup>6</sup>J. N. Schulman and T. C. McGill, *Appl. Phys. Lett.* **34**, 663 (1979).
- <sup>7</sup>J. R. Meyer, C. A. Hoffman, F. J. Bartoli, J. W. Han, J. W. Cook Jr., J. F. Schetzina, X. Chu, J. P. Faurie, and J. N. Schulman, *Phys. Rev. B* **38**, 2204 (1988).
- <sup>8</sup>E. R. Youngdale, C. A. Hoffman, J. R. Meyer, F. J. Bartoli, X. Chu, J. P. Faurie, and J. N. Schulman, in *Technical Digest, Conference on Lasers and Electro-Optics, Anaheim, 1988* (unpublished).
- <sup>9</sup>K. A. Harris, S. Hwang, D. K. Blanks, J. W. Cook, Jr., J. F. Schetzina, N. Otsuka, J. P. Baukus, and A. T. Hunter, *Appl. Phys. Lett.* **48**, 396 (1986).
- <sup>10</sup>J. Reno, R. Sporcken, Y. J. Kim, C. Hsu, and J. P. Faurie, *Appl. Phys. Lett.* **51**, 1545 (1987).
- <sup>11</sup>J. N. Schulman, O. K. Wu, E. A. Patten, J. W. Han, Y. Lansari, L. S. Kim, J. W. Cook, Jr., and J. F. Schetzina, *Appl. Phys. Lett.* **53**, 2420 (1988).
- <sup>12</sup>F. J. Bartoli, C. A. Hoffman, and J. R. Meyer, *J. Vac. Sci. Technol. A* **4**, 2047 (1986).
- <sup>13</sup>A. C. Beer, *Galvanomagnetic Effects in Semiconductors* (Academic, New York, 1963), Sec. 12.
- <sup>14</sup>Magnetic distortion of the superlattice band structure may be relatively strong in narrow- and zero-gap HgTe-CdTe heterostructures. Fortunately, transport coefficients of the lightest-mass carriers for which the effect will be greatest are sensitive primarily to Hall and conductivity data at very low magnetic fields where the perturbation is weak. The densities and mobilities listed in Table I are probably affected only in second order. There is currently no theoretical formalism available for incorporating field-dependent effective masses into a mixed-conduction analysis.
- <sup>15</sup>W. A. Beck, F. Crowne, J. R. Anderson, M. Gorska, and Z. Dziuba, *J. Vac. Sci. Technol. A* **6**, 2772 (1988).
- <sup>16</sup>J. R. Meyer, C. A. Hoffman, F. J. Bartoli, J. M. Perez, J. E. Furneaux, R. J. Wagner, R. J. Koestner, and M. W. Goodwin, *J. Vac. Sci. Technol.* (to be published).
- <sup>17</sup>C. A. Hoffman, J. R. Meyer, F. J. Bartoli, X. Chu, and J. P. Faurie, in *Proceedings of the 19th International Conference on Physics in Semiconductors (Warsaw, 1988)*, edited by W. Zawadzki and J. M. Langer (DHN, Warsaw, in press).
- <sup>18</sup>Unpublished results.
- <sup>19</sup>For example, see C. Kittel, *Introduction to Solid State Physics* (Wiley, New York, 1971), p. 368.
- <sup>20</sup>M. W. Goodwin, M. A. Kinch, R. J. Koestner, M. C. Chen, D. G. Seiler, and R. J. Justice, *J. Vac. Sci. Technol. A* **5**, 3110 (1987).
- <sup>21</sup>E. A. Patten, K. Kosai, T. N. Casselman, J. N. Schulman, Y.-C. Chang, and J.-L. Staudenmann, *J. Vac. Sci. Technol. A* **5**, 3102 (1987).
- <sup>22</sup>E. Finkman and Y. Nemirovsky, *J. Appl. Phys.* **50**, 4356

- (1979).
- <sup>23</sup>J. Reno, I. K. Sou, J. P. Faurie, J. M. Berroir, Y. Guldner, and J. P. Vieren, *Appl. Phys. Lett.* **49**, 106 (1986).
- <sup>24</sup>R. Aggarwal (private communication).
- <sup>25</sup>J. R. Meyer, F. J. Bartoli, and C. A. Hoffman, *J. Vac. Sci. Technol. A* **5**, 3035 (1987).
- <sup>26</sup>M. I. D'yakonov and A. V. Khaetskii, *Fiz. Tekh. Poluprovdn.* **14**, 1499 (1980) [*Sov. Phys.—Semicond.* **14**, 891 (1980)].
- <sup>27</sup>Since the barriers are assumed to contain 15 mol % HgTe, the stated HgTe-CdTe valence-band offsets have been multiplied by 0.85 in the calculations.
- <sup>28</sup>Y. Guldner, G. Bastard, J. P. Vieren, M. Voos, J. P. Faurie, and A. Million, *Phys. Rev. Lett.* **51**, 907 (1983).
- <sup>29</sup>S. P. Kowalczyk, J. T. Cheung, E. A. Kraut, and R. W. Grant, *Phys. Rev. Lett.* **56**, 1605 (1986).
- <sup>30</sup>Tran Minh Duc, C. Hsu, and J. P. Faurie, *Phys. Rev. Lett.* **58**, 1127 (1987).
- <sup>31</sup>J. N. Schulman and Y.-C. Chang, *Appl. Phys. Lett.* **46**, 571 (1985).
- <sup>32</sup>J. M. Perez, R. J. Wagner, J. R. Meyer, J. W. Han, J. W. Cook, Jr., and J. F. Schetzina, *Phys. Rev. Lett.* **61**, 2261 (1988).
- <sup>33</sup>For example, D. L. Long and J. L. Schmit, *Semiconductors and Semimetals*, edited by R. K. Willardson and A. C. Beer (Academic, New York, 1970), Vol. 5, Chap. 5.
- <sup>34</sup>Nearly equal electron and light-hole masses in the Hg<sub>1-x</sub>Cd<sub>x</sub>Te alloy do not lead to equal mobilities, because the light holes are strongly scattered into a high density of heavy-hole final states. Lifting of the band degeneracy due to quantum confinement and strain may remove the strong interband coupling in the superlattice.
- <sup>35</sup>With increasing well thickness the hole dispersion at  $k_z=0$  eventually becomes "electronlike" (note the negative slope in Fig. 9).
- <sup>36</sup>J. M. Berroir and J. A. Brum, *Superlatt. Microstruct.* **3**, 239 (1987).
- <sup>37</sup>G. Y. Wu and T. C. McGill, *Appl. Phys. Lett.* **47**, 634 (1985).
- <sup>38</sup>The reciprocity between light (heavy) mass in the plane and heavy (light) mass in the growth direction is analogous to a similar heavy (light) reciprocity for anisotropic hole masses in stressed germanium [J. C. Hensel and K. Suzuki, *Phys. Rev. B* **9**, 4219 (1974)].
- <sup>39</sup>F. Thiele, U. Merkt, J. P. Kotthaus, G. Lommer, F. Malcher, U. Rossler, and G. Weimann, *Solid State Commun.* **62**, 841 (1987).
- <sup>40</sup>D. L. Rode and J. D. Wiley, *Phys. Status Solidi B* **56**, 699 (1973).
- <sup>41</sup>J. G. Broerman, *Phys. Rev. B* **1**, 4568 (1970).